Dalton Transactions

PAPER

CrossMark
click for updates

Understanding the Zr and Si interdispersion in $Zr_{1-x}Si_xO_2$ mesoporous thin films by using FTIR and XANES spectroscopy†

Leandro Andrini,[a] Paula C. Angelomé,*[b] Galo J. A. A. Soler-Illia[c,d] and Félix G. Requejo[a,e]

Zr–Si mixed mesoporous oxides were obtained in a wide range of proportions, from 0 to 30% and from 70 to 100% of Si, using $Si(OEt)_4$ and $ZrCl_4$ as precursors and Pluronic F127 as a template. The oxide mesostructure was characterized by transmission electron microscopy and 2D-small angle X-ray scattering. Fourier transform infrared spectroscopy measurements suggested a local homogeneous interdispersion of both cations. Further selective studies using X-ray Absorption Near Edge Structure (XANES) spectroscopy for separately Zr and Si local environments, allowed for demonstrating that the Zr coordination varies from close to 7 to 6, when its concentration in the mixed oxide is reduced. In addition, it was possible to determine that in mixed oxides with low Zr concentrations, Zr can fit into the spaces occupied by Si in SiO_2 pure oxide. An equivalent XANES result was obtained for Si, which is also compatible with the information obtained by FTIR. Furthermore, the Zr–O distance varied from close to 2.2 Å to 1.7 Å when the Zr concentration decreased. Finally, our study also demonstrates the usefulness of XANES to selectively assess the local structure (coordination, symmetry and chemical state) of specific atoms in nanostructured systems.

I. Introduction

Materials displaying organized mesoporosity (pore diameters in the 2–50 nm range) have gained enormous interest in recent years, due to their high potential for application in areas such as catalysis, controlled drug delivery, spatially controlled nanoreactors, sensors, etc.[1,2] These materials are prepared by combining sol gel reactions and self-assembly of amphiphilic templates that, upon elimination, give rise to ordered pore arrays.

Since the first reported synthesis, in 1992 (mesoporous SiO_2 known as MCM41)[3] a huge variety of materials such as oxides, phosphates, nitrides, sulfides and carbons have been syn-

thesized, and the field can be considered mature.[2] In particular, mesoporous oxides can be routinely obtained as powders, aerogels, fibers and films by just changing the synthesis conditions. The Evaporation Induced Self Assembly – EISA – approach[4] is a flexible route to generate mesoporous films, xerogels, monoliths or aerosol particles through a drying process.[5] Mesoporous thin films are currently being explored as advanced coatings, sensors, optoelectronic devices and easily separable catalysts.[6]

Zirconia–silica mixed oxides result to be very attractive due to their interesting properties such as mechanical strength, chemical durability, low thermal expansion, tuneable refractive index, etc.[7] Because of all these characteristics, these oxides have gained great technological and basic interest and are currently being used as ceramic materials,[8] catalysts,[9,10] optoelectronic devices,[11] dielectrics,[12] and for separation.[13] Addition of a high surface area and organized porosity to these mixed oxides opens up new possibilities, as the obtained materials present a higher accessible surface for exchange, which is of particular importance for catalysts, catalyst supports or materials for separation. In addition, the difference in acidity of both cations permits to tune the surface speciation of these oxides, which leads to controlling the adsorption, chemical selectivity or catalytic activity practically at will.

From the synthetic point of view, Zr(IV) and Si(IV) cations show dissimilar hydrolysis/condensation behaviour in sol–gel

[a]Instituto de Investigaciones Fisicoquímicas Teóricas y Aplicadas, INIFTA - CONICET, 1900 La Plata, Argentina
[b]Gerencia Química, Centro Atómico Constituyentes, Comisión Nacional de Energía Atómica, Av. General Paz 1499, B1650KNA San Martín, Buenos Aires, Argentina. E-mail: angelome@cnea.gov.ar
[c]Departamento de Química Inorgánica, Analítica y Química Física, Facultad de Ciencias Exactas y Naturales, Universidad de Buenos Aires, Buenos Aires, Argentina
[d]Instituto de Nanosistemas, Universidad Nacional de General San Martín, Av. 25 de Mayo y Francia, 1650 San Martín, Buenos Aires, Argentina
[e]Departamento de Física, Facultad de Ciencias Exactas, Universidad Nacional de La Plata, La Plata, Argentina
†Electronic supplementary information (ESI) available. See DOI: 10.1039/c6dt00203j

reactions.[1,9] This is a limitation for obtaining mixed oxides with a high level of interdispersion, a central aspect that plays a critical role on the final optical, catalytic or separation properties of mixed oxides. Thin films,[14,15] aerogels[16,17] and powders[18–23] of Zr–Si mixed oxides with different Zr : Si proportions have been obtained previously. However, even if these studies have proven the existence of highly interdispersed amorphous mixed phases, in most of them there was a lack of detailed information on the macroscopic, mesoscopic and local structures of the ions in the oxides.

It is well known that Zr(IV) cannot isomorphically substitute Si(IV) in silicate minerals due to its large size and high charge,[24] which leads to mostly amorphous Zr–Si mixed oxides at low temperatures, the local structure of which is interesting from the fundamental point of view. Additionally, the Zr–silicate ($ZrSi_xO_y$) formation between ZrO_2 and SiO_2 remains a serious technological problem to solve, and the Zr–silicate is relevant because the presence of this stable species passivates the Zr–Si mixed oxide properties.[25] Crystalline Zr–silicate ($ZrSiO_4$, zircon) is usually formed at temperatures higher than 1400 °C,[26] but there are no systematic studies at the nanoscale that evidence that its formation can be promoted, and thus it becomes necessary to determine the presence of this phase by an adequate method.

The crystal structure of ionic materials can be determined by radius-ratio rules,[27] and because of the small size of the Zr^{4+} ions, these rules place ZrO_2 on the border between the 8-fold coordinated fluorite structure and the 6-fold co-ordinated rutile one.[28] For example, zirconium, in glass–crystal composite materials, can be found in 6- or 7-fold coordinated sites.[29,30] Besides its technological implications, the relationship between these structures is of fundamental interest.[28,31–34] Consequently, the local and/or extended crystalline structure has implications on the material properties and therefore it is very important to have both a reliable synthesis method that allows controlling the Zr coordination number, as suitable methods for experimental characterization of this parameter.

In this work, we synthesized, characterized and investigated in detail the ion local structure of large-pore mesoporous $Zr_{1-x}Si_xO_2$ thin films, with x ranging between 0 to 0.3 and 0.7 to 1.0. The main goal was to understand the effect of the Zr : Si molar relationship on the local ion structure and the homogeneity of the inorganic framework. We have substantially improved the more traditional characterization methodologies for these kinds of samples (Fourier Transform Infrared Spectroscopy – FTIR, Transmission Electron Microscopy – TEM, 2D-Small Angle X-Ray Scattering – 2D-SAXS) by using X-ray Absorption Spectroscopy (XAS), a powerful technique for obtaining information on absorbing atom and its local environment.[35] In particular, X-ray Absorption Near Edge Structure (XANES) was used at both L2,3 and K Zr and Si absorption edges respectively. This technique is strongly sensitive to chemistry (formal oxidation state and local geometry), p–d hybridization, electronic arrangement and the density of available unoccupied electronic states of the absorbing

atom.[36,37] In addition, the Zr L-XANES splitting can be used to determine Zr–O average distances as a function of Zr concentration, by applying crystal field theory.

II. Experimental

Sample preparation

Mesoporous $Zr_{1-x}Si_xO_2$ mixed oxide thin films were prepared by Evaporation-Induced Self Assembly (EISA) under controlled deposition conditions, as previously reported for pure[38,39] and mixed Zr–Si and Ti–Si mesoporous oxide thin films.[14,40] Non-ionic triblock copolymer Pluronic F127 ($[EO]_{106}[PO]_{70}[EO]_{106}$; EO = ethylene oxide, PO = propylene oxide), that gives rise to pore diameters in the 6–8 nm range, was used as the template.

The sol composition was $ZrCl_4 : Si(OEt)_4 : H_2O : F127 : EtOH = 1 − x : x : 20 : 0.005 : 40$, with x varying between 0 and 0.3 (Zr rich range) and between 0.7 and 1 (Si rich range). Direct mixing of all components led to mesoporous films with homogeneous walls albeit locally ordered mesopores. All sols were transparent and stable at ambient temperature, and can be re-used several times if conserved in a freezer at −18 °C, and gently restored to room temperature prior to use.

Precursor solutions were used to produce mesoporous thin films by dip-coating onto FTO (Fluorine Tin Oxide) covered glass substrates, under 20% relative humidity at 25 °C, with a withdrawing rate of 2 mm s$^{−1}$. Immediately after their preparation, the films were subjected to a short water vapor treatment[14] and then subjected to subsequent 24 hour treatments at 50% relative humidity, 60 °C and 130 °C to improve cross-linking of the inorganic network, and favor the formation of ordered micellar arrays. Thermal treatment of these stabilized coatings (up to 350 °C, 2 hours) was performed in a tubular oven, under still air, using a 1 °C min$^{−1}$ temperature ramp.

The films were labeled as ZSab where ab represents the molar proportion between Zr and Si in the mixed oxide. For example, a film containing 80% of Zr and 20% of Si was called ZS82.

Mesostructure and chemical characterization

The film mesostructure was characterized by Small Angle X-Ray Scattering (2D SAXS) at the D02A-SAXS2 line at the Laboratorio Nacional de Luz Síncrotron LNLS (Campinas, SP, Brazil),[41] using λ = 1.608 Å, a sample–detector distance of ~690 mm, and a CCD detector (3° incidence). For these measurements the samples were deposited onto coverslip glasses and treated at 200 °C instead of 350 °C.

TEM images were collected using a Philips EM 301 transmission microscope (CMA, FCEyN, UBA) operated at 60 kV or a Philips CM 200 Super Twin (GM, CAC, CNEA) operated at 200 kV and equipped with EDAX®. Samples were obtained by scratching the films from the substrate and deposited on carbon coated copper grids.

FTIR spectra were recorded on a Nicolet Magna 560 instrument, equipped with a liquid nitrogen cooled MCT-A detector. For analysis, the films were directly deposited onto Si wafers

(University Wafer, South Boston, MA), which are transparent in the IR region of interest.

XANES measurements and data processing

The Zr L2–L3 and Si K-edge XANES measurements were carried out at the D04A-SXS beamline at LNLS[42,43] (Campinas, SP, Brazil). Synchrotron radiation was monochromatized by using a double-crystal monochromator equipped with InSb-(111) crystals giving an energy resolution of 2.2 eV at the Zr L2–L3-edge, and 1.3 eV at the Si K-edge. The beam focalization was performed using a spherical Rh mirror. The incident photon energy was in the range of Zr L2–L3 and Si K-edges for the corresponding absorption experiments. The I_0 beam intensity was measured using a thin foil of Al located before the main chamber. The XANES spectra were recorded in total electron yield (TEY) mode, collecting the emitted current, for each photon-energy, with an electrometer connected to the sample. The photon energies were calibrated using a Zr or Si metallic foil and setting the first inflection point to the energy of the Zr-L2 (2307 eV) and Zr-L3 (2223 eV) absorption for Zr^0, and the Si K absorption edge for Si^0 (1839 eV).

Two polynomial functions were fitted to reduce the background and normalize the spectra at both Zr L2–L3 and Si K-edges: one for the pre-edge region and the second one for the region beyond the edge. After background subtraction and normalization, the white line (WL) region was fitted using Gaussian peak functions and the continuum step was fitted using arctan functions.[44] For this purpose, the WinXAS3.1 program was used.[45]

III.   Results and data analysis

Macroscopic and mesoscopic characterization

The mesoporous mixed oxide thin films were prepared by dip-coating under controlled conditions followed by gentle post-processing. As demonstrated previously[14] it is essential to control the hydrolysis and condensation behavior of Zr(IV) and Si(IV), towards controlling the order at two length scales: (a) molecular (associated with homogeneity of the walls) and (b) mesoscopic (associated with the order of monodisperse pore arrays). After some preliminary tests using different precursors and pre-treatments of the sols, the best conditions were chosen: the sols were prepared by directly mixing $ZrCl_4$ and $Si(OEt)_4$. $Zr_{1-x}:Si_xO_2$ appropriately interdispersed mixed oxides were obtained in the $0 \leq x \leq 0.3$ and $0.7 \leq x \leq 1$ ranges.

The obtained films present different mesopore structures, as can be seen in the TEM pictures and 2D-SAXS patterns in Fig. 1 and in the information presented in Table S1 (ESI†): a mixture of well-ordered $Fm\bar{3}m$ and $Im\bar{3}m$ cubic phases for $x < 0.3$, and cubic $Im\bar{3}m$ for $x = 1$, and locally ordered mesopores for the rest of the compositions. However, in all samples the interplanar distances between the mesopore planes are around 12 nm, as expected for mesoporous materials templated with Pluronic F127.

In addition, all samples appeared homogeneous under TEM observation, *i.e.* with no sharp changes in contrast due to phase segregation.[14] Finally, the Zr:Si ratio estimated by EDS presented similar values along the samples within 5–10% error, as can be seen, as an example, for the ZS37 sample in Fig. 1c.

The TEM images, complemented with the EDS results were the first evidence to prove the framework homogeneity. In fact, TEM allowed determining that the sample prepared with 50% of Si and 50% of Zr (ZS55) was not homogeneous (Fig. S1, ESI†).

FTIR has been proven to be a reliable technique in order to study the chemical bonds in mixed metal oxides containing Si[14,40] and was performed in the samples that have a homogeneous appearance under TEM. All the spectra were obtained before and after thermal treatment and thoroughly analyzed in the 1500–700 cm^{-1} region. Fig. 2 shows the FTIR spectra of
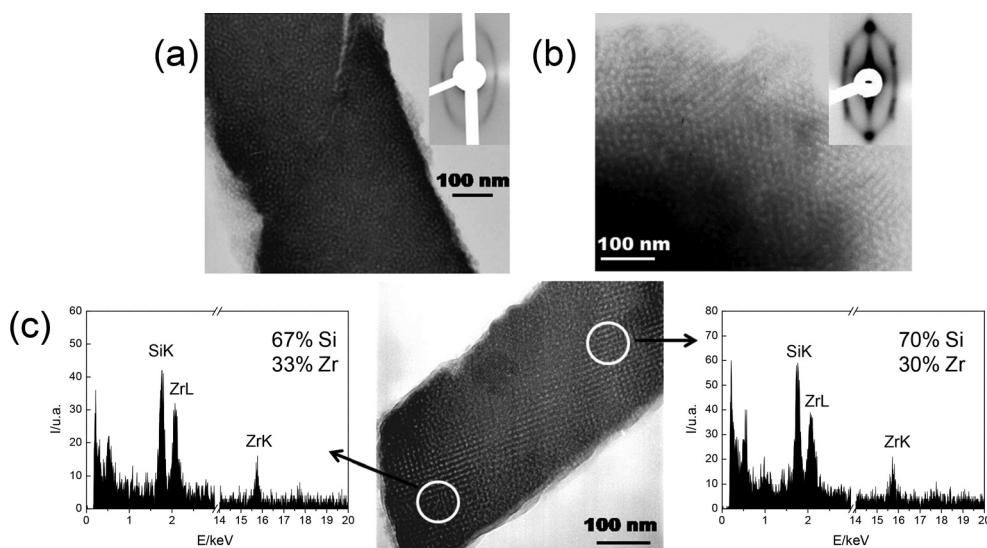

Fig. 1 TEM and 2D-SAXS characterization (inset) of $Zr_{1-x}Si_xO_2$ mesoporous mixed oxides: (a) ZS28 (x = 0.8) locally organized pore structure, (b) ZS82 (x = 0.2) cubic mesostructure, and (c) TEM of the ZS37 (x = 0.7) cubic sample, showing two EDS spectra obtained at different sample locations.
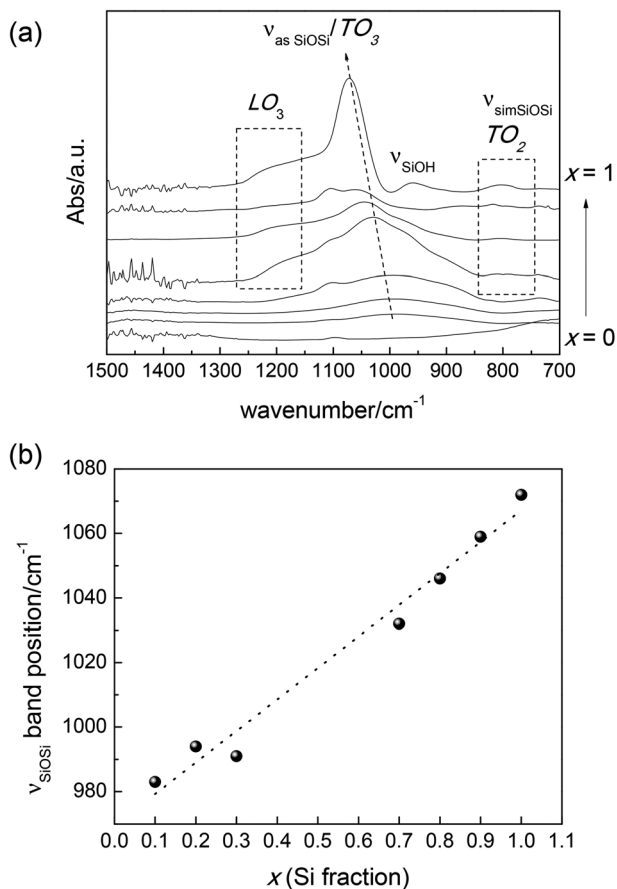
Fig. 2 (a) FTIR absorption spectra in the 700–1500 cm^{-1} region for mixed oxide thin films treated at 350 °C. Compositions and significant bands are indicated in the figure. (b) Evolution of the asymmetric Si–O–Si TO$_3$ band position as a function of the Si fraction, x, for samples shown in (a).

both mixed oxide samples and pure oxide standards treated at 350 °C, with band assignation according to the literature.[46] Three bands associated with the Si–O–Si bonds are observed: longitudinal optical modes LO$_3$ at ~1200 cm^{-1}, $\nu_{asSiOSi}$ (TO$_3$) at ~1050 cm^{-1} and $\nu_{symSiOSi}$ (TO$_2$) at ~800 cm^{-1}. A band associated with ν_{SiOH} is also observed at 950 cm^{-1} for the samples containing a high Si concentration.

As the Si proportion increases, two main trends are observed in the spectra: an increase in the intensity of the $\nu_{symSiOSi}$ band and a shift of the $\nu_{asSiOSi}$ band to higher wavenumbers. The first trend has been attributed to the disruption of the order in the SiO$_2$ framework,[47] as the Zr concentration increases. This observation points towards a good interdispersion in the mixed oxide, as only in this case a progressive change in the FTIR spectra is expected.

The second observation, the displacement of the $\nu_{asSiOSi}$ band to lower wavenumbers as the Zr proportion increases, is coincident with previous observation presented both in the mixed oxide literature[48–50] and in previous work performed in mesoporous mixed titania–silica oxides.[40] It has been proposed that the position of the Si–O–Si asymmetric vibration is

an indicator of the oxide dispersion.[40] This observation is related to the change in the oscillator's reduced mass that gives rise to the FTIR signal. That is, if Si is replaced with Zr uniformly, the Si–O–Si bonds are converted into Zr–O–Si bonds, so the oscillator's reduced mass increases and, therefore, the bond vibration frequency decreases. If the oxides are well interdispersed, it is expected that the band position follows a linear relationship with the Si proportion in the mixed oxide.[48] This is, in fact, what is observed in the studied samples, as shown in Fig. 2b.

XANES characterization

The TEM and FTIR results presented in the previous sections suggest that the inorganic mixed oxide framework is highly interdispersed at the macroscopic and mesoscopic levels. However, the actual local environment, cation intermixing at the molecular level and electronic structure of the Zr and Si atoms cannot be determined by these techniques. Techniques based on X-ray absorption spectroscopy are ideal to study an atomic local environment (within about 6 Å), as they allow for obtaining information about the closest environment of a selected element. Besides, data interpretation does not rely on any symmetry or periodicity requirement.[51] In particular, the structural information obtained from XANES is useful for identifying the chemical speciation of a particular element, selected by the incident photon energy used. Thus, the local environment and electronic structure of both Zr and Si atoms in all the mixed oxides were selectively characterized and analysed by means of XANES.

Zr L2–L3. Since the XANES region of the X-ray absorption process is strictly and strongly related to both the symmetry and electronics of the absorbing element, the Zr L2–L3 edges can give sensitive short and medium range structural and bonding information. XANES allows a direct comparison, *i.e.* a finger-print method, between the sample spectra and relevant standards, revealing unique spectral features and giving an idea of possible chemical species represented in the sample.[51,52]

Representative Zr L2–L3-edge XANES spectra obtained for reference compounds are shown in Fig. 3a. ZrO$_2$ can form cubic, tetragonal, and monoclinic phases or orthorhombic phases at high pressures. In tetragonal (t) ZrO$_2$ the first environment oxygen atoms are highly distorted and the coordination varies between 7 and 8. In stabilized cubic (c) ZrO$_2$, Zr is 7-coordinated to oxygen atoms ($^{[7]}$Zr).[53] For ZrO$_2$ monoclinic (m) and amorphous (a), Zr is 7-coordinated to oxygen atoms. In BaZrO$_3$, Zr is 6-coordinated to oxygen atoms ($^{[6]}$Zr) and the split is well resolved. In ZrSiO$_4$, Zr is 8-coordinated ($^{[8]}$Zr) and the splitting is not perceived.[29]

Fig. 3b shows experimental (hollow circles) Zr L3 XANES for BaZrO$_3$ and m-ZrO$_2$, and the fit (full line) of the experimental data. The scheme in Fig. 3c shows the 4d-orbital splitting for the 2p$_{3/2}$ → 4d transition in a crystal field with octahedral or tetrahedral symmetry. The two Gaussians used to adjust the data in Fig. 3b, are attributed to the 2p$_{3/2}$ → 4d(t$_{2g}$) transition and 2p$_{3/2}$ → 4d(e$_g$) transition. Even if the representation
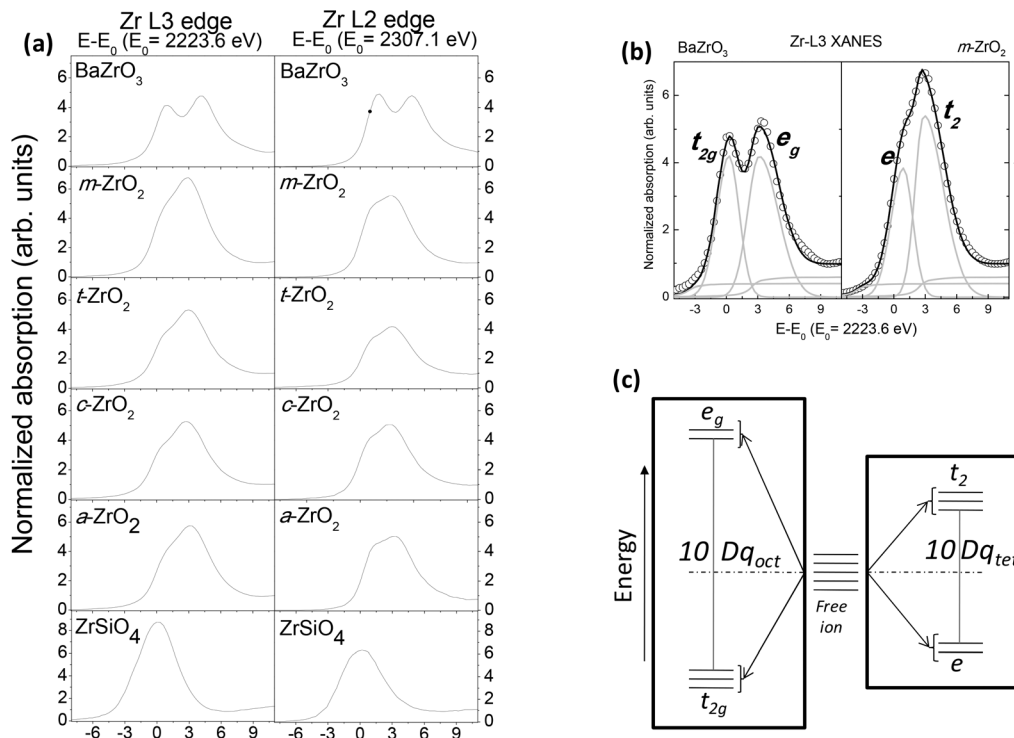
Fig. 3 (a) Zr L3 and L2 XANES reference compounds. For example, in BaZrO$_3$, Zr is 6-coordinated ($^{[6]}$Zr), in m-ZrO$_2$ and a-ZrO$_2$, Zr is 7-coordinated ($^{[7]}$Zr) and in ZrSiO$_4$, Zr is 8-coordinated ($^{[8]}$Zr). Tetragonal and cubic ZrO$_2$ phases are shown for completeness. (b) Zr L3 XANES for BaZrO$_3$ ($^{[6]}$Zr), t_{2g}–e_g identification with 10Dq crystal field split in the O_h symmetry; and Zr L3 XANES for m-ZrO$_2$ ($^{[7]}$Zr) t_2–e identification with the T_d symmetry. (c) Simple scheme of 4d-orbital splitting for the 2p$_{3/2}$ → 4d transition.

names t_{2g} and e_g are valid only for the cubic O_h point group, for simplicity, and to keep only one parameter for the crystal field visible in the experiment, we maintain the same notations. The difference in energy between 4d(t_{2g}) and 4d(e_g) orbitals is defined as the crystal field parameter 10Dq (Fig. 3c).[54] Splitting empirical values (2p$_{1/2}$/2p$_{3/2}$ to 4d) were extracted from samples and references and are presented in Table 1.

Fig. 4 shows the experimental Zr L2–L3-edge XANES spectra for all the mixed oxide samples studied in this work and their

fits. A pronounced splitting in the L2–L3 absorption peaks is readily observed for the samples with lower molar Zr(IV) contents (0.7 ≤ x, i.e. ZS19, ZS28 and ZS37). An increase in the total intensity of the L2 absorption edge and a decrease in the total intensity of the L3 edge as the molar proportion of Zr increases are also observed. The structure of the spectrum can therefore be directly related to the exact crystal-field splitting.[55]

The Zr L2–L3 edges are due to 2p^{6}4d^n → 2p^{5}4d^{n+1} transitions, from a 2p core state to the empty states of both s and d characters. These states are separated by 3/2 times the core spin–orbit coupling, ξ_{2p}. For zirconium compounds this separation is in the order of 85 eV. Ideally, the intensity of the L3 edge (j_{core} = 3/2) is twice that of the L2-edge (j_{core} = 1/2). Within a single-particle scheme the only possibility of differences between the spectral shape of the L3 and L2-edges is the spin–orbit coupling of the valence electrons.[56] It is experimentally found that the L2 and L3 edges are often different (e.g., 4d systems: zirconium, molybdenum, niobium and ruthenium), and these differences are due to multiplet effects coupling the 2p core wave function to the valence states of 4d character.[56] It is also known that the L3 edge is more affected by the multiplet effects than the L2-edge.[57]

In the experimental results displayed in Fig. 4, it can be observed that the samples with lower Zr proportions present a splitting in the L2 (L3) edge due to the crystal-field interaction, and the relative heights of t_{2g}–e_g are reversed in the L3 edge
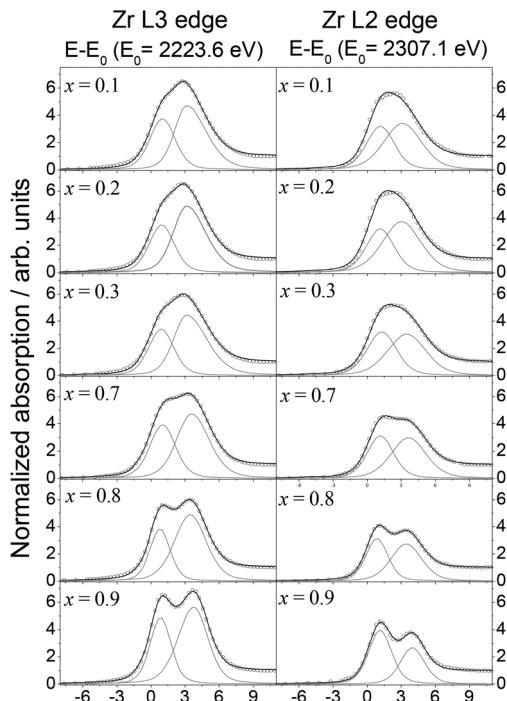
Table 1 Splitting (ΔE(L3) or ΔE(L2)) due to the crystal field

Reference compounds	ΔE(L3) (eV)	ΔE(L2) (eV)
BaZrO$_3$	2.9$_1$	3.0$_1$
m-ZrO$_2$	2.1$_1$	2.0$_1$
t-ZrO$_2$	2.2$_1$	2.1$_1$
c-ZrO$_2$	2.2$_1$	2.1$_1$
a-ZrO$_2$	2.1$_1$	2.1$_1$
SiZrO$_4$	1.7$_1$	1.6$_1$
Samples-x Si fraction	ΔE(L3) (eV)	ΔE(L2) (eV)
ZS19-0.9	2.8$_1$	2.8$_1$
ZS28-0.8	2.7$_1$	2.7$_1$
ZS37-0.7	2.4$_1$	2.5$_1$
ZS73-0.3	2.2$_1$	2.1$_1$
ZS82-0.2	2.1$_1$	2.1$_1$
ZS91-0.1	2.1$_1$	2.0$_1$

Fig. 4 Zr L3 and L2 XANES of the mixed oxide samples (x = Si fraction), without arctan functions for simplicity.

Fig. 5 Splitting value ΔE (L3) *vs.* x (% Si fraction) in the samples.

from the L2-edge. This evidences that the Zr content in the mixed oxide affects the electronic Coulomb exchange interaction.[29,52,58] In the case of samples with $x \leq 0.3$, the shape of the Zr L2–L3 XANES spectra is similar to the a, m, t and c ZrO$_2$ oxide references shown in Fig. 3. This might suggest a similar electronic behavior; however, it has been reported that differences can arise between the electronic structure of the tetragonal and cubic ZrO$_2$ phases.[59] In addition, it is also known that there is a dependence of the electronic structure on the lattice parameters of these types of oxides.[59,60]

Our experimental results clearly show that the splitting of the Zr 4d orbital into the t$_{2g}$ and e$_g$ states varies as a function of the zirconium percentage in the oxide (Fig. 5). The tendency can be divided into two regions: one for a low Zr concentration (high x) and one for a high Zr concentration (low x). In the low x samples, the Zr environment is close to the one in zirconium oxides, and the electrostatic and electronic perturbations due to the presence of silicon are minor. On the other hand, in the Si-rich phases, the coordination sphere of Zr is more strongly affected along the Si increase. By extrapolating the linear fit of these two regions, an intersection in the region corresponding to the ratio Zr : Si ≈ 0.45 is obtained. This can be interpreted as the existence of a "phase transition". In what follows we will see that this "phase transition" corresponds to the change in average distances, nearest neighbours and average number of nearest neighbours of the Zr cation. Noteworthily, the ratio Zr : Si = 0.5 could not be obtained experimentally under our synthesis conditions, as phase separation occurred (see Fig. S1, ESI†). We can speculate that the crystal field allows for
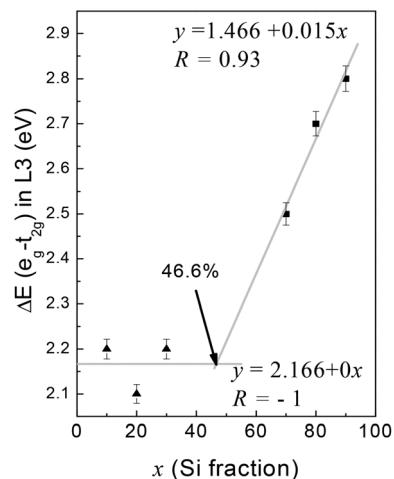
the formation of a well-dispersed mixed oxide whenever Zr : Si concentrations deviate enough of 0.5.

Morinaga *et al.*[59] argue that as the distance between the Zr and O ions decreases, the electrostatic field becomes larger, and the bond becomes more ionic. The bond order and the magnitude of the energy gap between the highest occupied O-2p level and the lowest unoccupied Zr-4d level also depend on the crystal structure. These changes in the electronic states seem to be closely related to the phase stability of ZrO$_2$.[59]

The 10Dq parameter of the crystal field can be expressed analytically as a function of the distance from the oxide ligands to the central metal ion (R),[61] and this expression can be used to calculate R. The 10Dq parameter is proportional to $\frac{\langle r^4 \rangle}{R^5}$, where $\langle r^4 \rangle$ is the mean value of the fourth power of the radial distance of a d orbital from the nucleus and R is the distance from the ligands to the central metal ion.

It is known that the crystal field model is an approach that does not consider the bonds and valence states[61,62] and thus, presents some limitations. However, it can provide approximated information from local arrangement of the inorganic materials investigated.[63] In this case the local crystal field parameter of the mixed oxides can be compared with the crystal field parameters of reference compounds. Considering $\langle r^4 \rangle \sim 20a_0^4$ ($a_0 \sim 0.5$ Å),[63,64] and a regular array of neighbouring atoms,[61] the approximated distance between ligands and the Zr ion can be obtained and compared with the distances to the first neighbouring O in m-ZrO$_2$, in the 2p$_{1/2}$ to 4d transitions. Proposing a Zr–O average distance, d, of 2.18 Å (ref. 65) for the monoclinic oxide m-ZrO$_2$, the following average distances were obtained: $R_{ZS19} = 1.7_2$ Å; $R_{ZS28} = 1.7_2$ Å and $R_{ZS37} = 1.9_2$ Å. Thus, the relationship d(Zr–O)$_{ZS19}/d$(Zr–O)$_{m-ZrO_2}$ is approximately 0.8 for the samples with lower molar concentrations of Zr. For the samples with higher molar concentrations of Zr, the obtained distances are similar to the average Zr–O distance in m-ZrO$_2$ and amorphous a-ZrO$_2$. Amorphous

SiO_2 has a tetrahedral nearest neighbour's arrangement of oxygen at 1.61 Å (ref. 66) (or 1.62 Å (ref. 67) for SiO_2-glass). According to the average Zr–O distances obtained, it can be inferred that the Zr surrounded by a large amount of Si (as in the ZS19 sample) is morphologically forced to adopt a configuration similar to the one of SiO_2, by reducing the distance of the first neighbouring oxygen.

From a linear approximation relationship between $10Dq$ and the coordination number of reference compounds, the average coordination number of each sample can be obtained. Fig. 6 shows a decrease in the number of oxygen neighbours from 8 to 6 when the Zr concentration decreases. In addition, as the Zr concentration decreases, the average distance and the average number of oxygen neighbours decreases. In SiO_2, the Si site is tetrahedrally coordinated. These results suggest that in these systems, the Zr is occupying Si sites when present in low proportions.[68] A similar result was observed in mesoporous $Ti_{1-x}Si_xO_2$, in which at low Ti(IV) contents ($x > 0.8$), Ti substitutes Si in tetrahedral sites, the coordination increasing steadily for larger Ti : Si ratios.[40]

Our results are also consistent with the results in similar systems presented by L. Galoisy et al.,[29] L. Cormier et al.,[30] Mountjoy et al.,[69] Pickup et al.[70] and Gaultois et al.[71] And the 6-fold evidence is in agreement with the previous results reported in the papers of L. Galoisy et al.,[29] H. Ikeno et al.,[52] C. Patzig et al.,[58] P. E. R. Blanchard et al.,[72] and L. Cormier et al.[73]

The Zr L2–L3 XANES spectra show that there is a marked difference in the split for lower and higher molar Zr concentrations, and this splitting is not independent of the Zr molar concentration. Particularly since in 4d metals electrostatic interactions can be ignored compared to the spin–orbit interactions, there is a linear dependence between the branching ratio B_R and the spin–orbit interaction in the valence band.[74] Fig. 7 shows that $B_{R\ ZS91} < B_{R\ ZS19}$ (with $B_R = I(L3)/[I(L2) + I(L3)]$, where $I(Li)$ is the intensity of the white line, i.e. area, in the Li edge, with $i = 2, 3$). The B_R can be interpreted as the fraction of the total transition probability which fits into the $2p_{3/2}$ manifold, and it will be dependent on the spin distribution over the core-hole manifolds.[74] In 4d and 5d metals, the 2p–nd interactions are negligible compared to the 2p spin–orbit parameter, ξ_{2p} (2% and 0.2%, respectively), and the branching ratio measurements are also complementary to the measurements of magnetic susceptibility, electron paramagnetic resonance, and Mossbauer spectroscopy.[74]

The transition probability P is also affected by the molar concentration, which satisfies, for higher x, that $P(d^0 \to 2p_{1/2}^5 d^1) < P(d^0 \to 2p_{3/2}^5 d^1)$. That is, at low Zr molar concentrations, the $2p_{3/2}$ transitions are favoured versus the $2p_{1/2}$ transitions (i.e., the $I(L2)$ intensity is lower for higher x concentrations, see Fig. 4). According to the probability ratio, these materials promote a transition over another, leading to the possibility of exploring the characteristics of selectivity or preference of certain electronic "de-excitation" pathways for $2p_{3/2}$ electrons.

In summary, by using the Zr L2–L3 XANES technique, we could demonstrate that the Zr-coordination diminishes (7-fold to 6-fold) when the Zr fraction is low ($0.7 < x$, where x is the Si fraction), the Zr–O distance decreases as the Zr concentration decreases, and there is evidence of a preferential channel for electronic "de-excitation" pathways for $2p_{3/2}$ electrons. In addition, using XANES as a fingerprint method, we could demonstrate that no zircon ($ZrSiO_4$) phase is present.
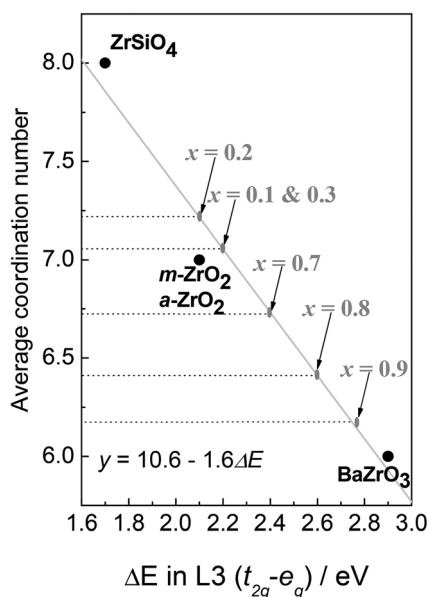

Fig. 6 Average coordination number as a function of the ΔE (L3) splitting value. It is observed that for higher x, the average coordination number tends to be 6.
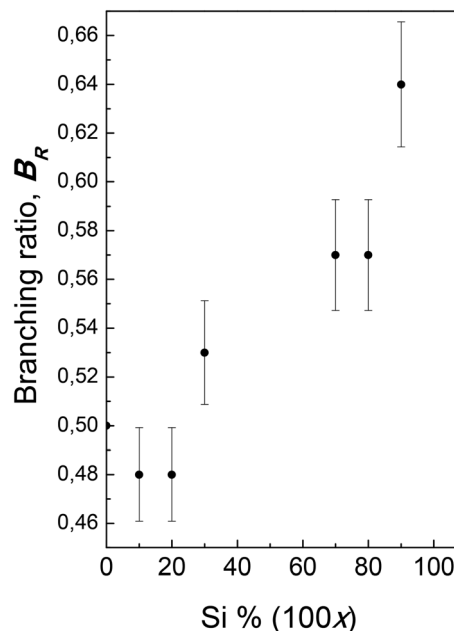

Fig. 7 Branching ratio, $B_R = I(L3)/[I(L2) + I(L3)]$, as a function of Si fraction.
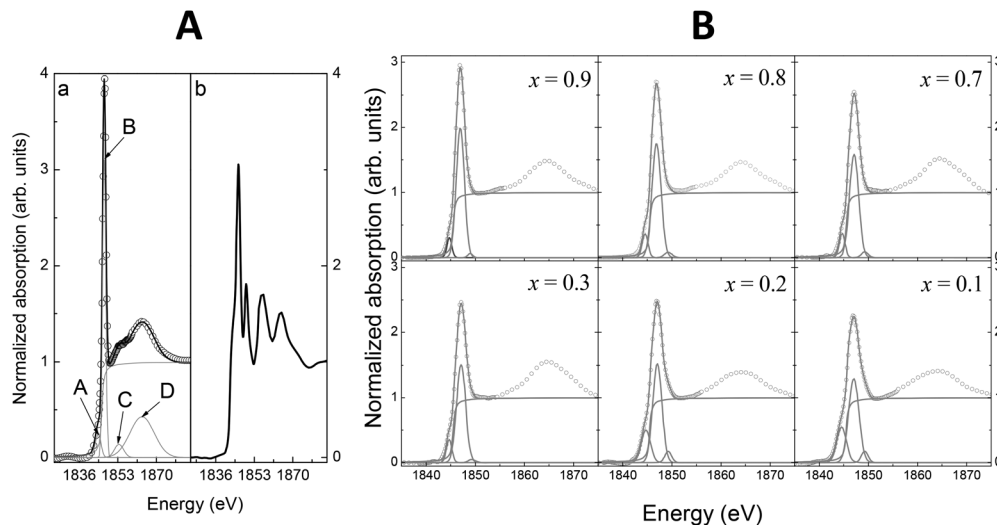
Fig. 8 (A) Si K XANES of reference samples: supported amorphous SiO_2 (a), and $ZrSiO_4$ (b). (B) Si K XANES experimental spectra for the Zr–Si samples with different x (Si fractions).

Si K. Fig. 8A(a) shows the Si K XANES experimental spectrum for amorphous SiO_2 supported on FTO (circles) and its fit using the Gaussian functions and arctan (solid lines). In this work we adopt the same assignment feature proposed by D. Li *et al.*[75] The first Gaussian (A), whose centroid is located at 1844.34 eV, is attributed to the transition of Si 1s electrons to the antibonding 3s-like state (a_1); this transition is forbidden by the dipole selection rules $\Delta L = \pm 1$, $\Delta S = 0$ and $\Delta J = \pm 1$, so that peak A is very weak. The second Gaussian for the most intense peak of the spectrum (B, white line) is centred at 1847.05 eV. This peak corresponds to the transition of Si 1s electrons to the antibonding 3p-like state (t_2) and this transition is allowed by the selection rules. The third Gaussian (C), at 1853.50 eV, appears due to the transition 1s → e(Si 3d–3p). Finally, the fourth Gaussian (D) it is located at 1863.66 eV and it corresponds to the transition 1s → t_2(Si 3d–3p). The observed transitions and its positions are in good agreement with the previously reported results, within the experimental error (see ref. 75 and references cited therein). Fig. 8A(b) shows the Si K XANES experimental spectrum for $SiZrO_4$. The differences between the two spectra (a and b) are clearly observed and can be used to detect the presence of some of these phases in the spectra of the mesoporous mixed oxide samples.

Fig. 8B shows the Si K XANES experimental spectra for all the prepared mixed oxides samples. A comparison of these spectra with the references indicates that no zircon ($ZrSiO_4$) phase is present. It can also be clearly observed that the density of empty states Si 1s → t_2 is affected by the presence of Zr as the white line area decreases as the concentration of Zr increases from $x = 0.9$ to $x = 0.1$. In fact, Fig. 9 shows that the area of the Gaussian B (defined in Fig. 8A(a)) depends on the Zr molar proportion in the sample. The changes are noticeable in the white line (Gaussian B), which is a dipole transition selection rule allowed by 1s → t_2. This transition allows a direct measurement of the population of holes in the Si valence band, which is clearly affected by the presence of Zr. Preliminary calculations by the B3LYP hybrid functional implementing the program FIREFLY, with pseudopotentials (LANL2DZ) for electrons of Si and Zr and basis double-ζ for Si, Zr, O and H valence electrons keeping the frozen geometries, indicate that the Si-3p unoccupied states decrease with the increasing proportion of Zr.[76]
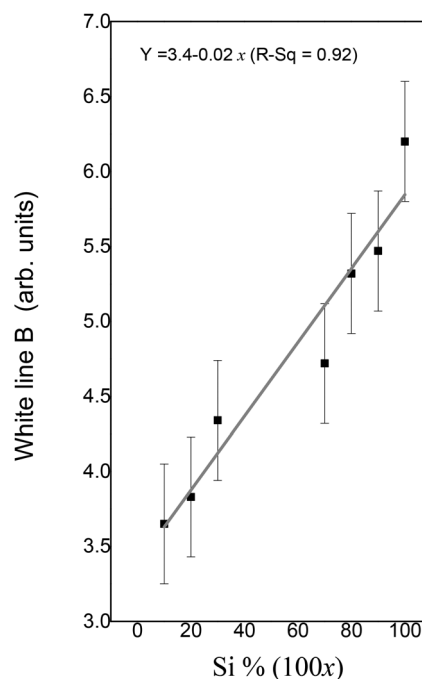

Fig. 9 White line areas (1s → 3p transition) as a function of the % Si molar fraction. The area of the amorphous SiO_2 white line used as a reference ($x = 1$) is introduced for comparison.

On the other hand, the Gaussian A is attributed to a forbidden transition by selection rules, and is associated with broken symmetries (*e.g.*, distortions). Therefore this peak in the XANES spectrum is associated with the local Si symmetry environment. Because this peak increases as the amount of Zr does, it can be deduced that the Si environment changes from a regular tetrahedron to a non-regular tetrahedron as more Zr is introduced in the mixed oxide, reinforcing the facts that point to an intimate mixture between the two cations. These results are in agreement with the results obtained by G. Mountjoy *et al.* by using neutron and X-ray absorption. These authors observed that the distribution of Zr in the absence of phase segregation causes more distortion of the SiO_2 network than the phase separation of ZrO_2 for large Zr concentrations.[69]

Finally, it is important to note that although FTIR gives information about bond vibrations and XANES about the electronic structure of absorbing atoms, the Si K XANES results shown here are compatible with the information obtained by infrared spectroscopy. As has been discussed previously, the band position of the Si–O–Si vibration in FTIR is affected by the introduction of Zr in the mixed oxide, indicating a change in the Si environment. This is fully in agreement with the results obtained by XANES, indicating the usefulness of both techniques to obtain selective information about the mixed oxide structures. Specifically we demonstrate by these experiments that all the obtained mixed mesoporous oxides are well interdispersed at the atomic level.

IV. Conclusions

In summary, homogeneous Zr–Si mixed mesoporous oxide thin films were obtained by EISA in a wide range of proportions (from 0 to 30% and from 70 to 100% of Si) and were characterized with several techniques, to understand the Si–Zr interdispersion.

The mesostructure order was demonstrated by both 2D-SAXS and electronic microscopy. TEM observations, supplemented with EDS, were the first step to prove the framework homogeneity at macroscopic and mesoscopic levels. In order to understand the chemical structure of the mixed oxides, FTIR and XANES spectroscopy were used. By FTIR it was possible to demonstrate the disruption of the order in the SiO_2 framework, as the Zr concentration increased. The Zr L2–L3 and Si K-edge XANES results were compatible with the information obtained by FTIR, but also offered quantitative data about changes in the environment of both cations.

The splitting of the Zr 4d orbital into the t and e states, obtained by Zr L2–L3 edge XANES, varied as a function of the zirconium percentage and is higher for the lower Zr concentrations. A simple linear model was used to follow the changes in the coordination number of Zr, which decreases from nearly 7 to 6 when the Zr concentration in the mixed oxide decreases. The Zr–O distance also decreases when the Zr content is lowered. On the other hand, Si K-edge XANES experiments showed that the density of empty states Si 3p–3s decreases as the concentration of Zr increases. This behavior is accompanied by a transition from a state of higher symmetry to a state of lower symmetry for the Si atoms, which indicates that Si adopts a different configuration as more Zr is introduced in the mixed oxide.

This work ultimately demonstrates the possibility of obtaining highly interdispersed Zr–Si mixed mesoporous oxides with a well local-defined environment for Zr and Si ions and the usefulness of the XANES technique as a characterization tool for these nanomaterials.

Finally, understanding the atomic structure of these kinds of mixed oxides helps to understand their chemical and physical properties and thus, their applications in fields in which a high surface area and tunable Brønsted acidity are needed such as catalysis, controlled delivery, cell scaffolds and separation.

References

1 G. J. A. A. Soler-Illia, C. Sanchez, B. Lebeau and J. Patarin, *Chem. Rev.*, 2002, **102**, 4093.
2 For a recent panorama of this field, see the special issue of *Chem. Soc. Rev.* 2013, **42**, 3649, guest edited by B. Lebeau, A. Galarneau and M. Linden.
3 C. T. Kresge, M. E. Leonowicz, W. J. Roth, J. C. Vartuli and J. S. Beck, *Nature*, 1992, **359**, 710.
4 C. J. Brinker, Y. Lu, A. Sellinger and H. Fan, *Adv. Mater.*, 1999, **11**, 579.
5 D. Grosso, F. Cagnol, G. J. A. A. Soler-Illia, E. L. Crepaldi, H. Amenitsch, A. Brunet-Bruneau, A. Bourgeois and C. Sanchez, *Adv. Funct. Mater.*, 2004, **14**, 309.
6 C. Sánchez, C. Boissière, D. Grosso, C. Laberty and L. Nicole, *Chem. Mater.*, 2008, **20**, 682.
7 A. Sawa, K. Nakanishi and T. Hanada, *Thin Solid Films*, 2008, **516**, 4665.
8 F. del Monte, W. Larsen and J. D. Mackenzie, *J. Am. Ceram. Soc.*, 2000, **83**, 628.
9 J. B. Miller and E. I. Ko, *J. Catal.*, 1996, **159**, 58.
10 Z. Wang, Y. Jiang, M. Hunger, A. Baiker and J. Huang, *ChemCatChem*, 2014, **6**, 2970.

11 Y. Yano and T. Noguchi, *US* 08/516356, 2008; Y. Yano and T. Noguchi, *US* 08/644,829, 2008.

12 F. Gonella, G. Mattei, P. Mazzoldi and G. Battaglin, *Chem. Mater.*, 1999, **11**, 814.

13 R. A. Shalliker and S. Kayillo, in *Encyclopedia of Chromatography*, Taylor & Francis, 3rd edn, 2009, p. 2444.

14 G. J. A. A. Soler-Illia, E. L. Crepaldi, D. Grosso and C. Sanchez, *J. Mater. Chem.*, 2004, **14**, 1879.

15 M. Lomoschitz, H. Peterlik, G. Friedbacher and U. Schubert, *J. Mater. Chem.*, 2009, **19**, 75.

16 Z.-G. Wu, Y.-X. Zhao and D.-S. Liu, *Microporous Mesoporous Mater.*, 2004, **68**, 127.

17 M. T. Bore, R. F. Marzke, T. L. Ward and A. K. Datye, *J. Mater. Chem.*, 2005, **15**, 5022.

18 D. Ortiz de Zárate, A. Gómez-Moratalla, C. Guillem, A. Beltrán, J. Latorre, D. Beltrán and P. Amorós, *Eur. J. Inorg. Chem.*, 2006, **2006**, 2572.

19 J. W. Kriesel, M. S. Sander and T. D. Tilley, *Adv. Mater.*, 2001, **13**, 331.

20 P. Yang, D. Zhao, D. I. Margolese, B. F. Chmelka and G. D. Stucky, *Nature*, 1998, **396**, 152; P. Yang, D. Zhao, D. I. Margolese, B. F. Chmelka and G. D. Stucky, *Chem. Mater.*, 1999, **11**, 2813.

21 S. Gontier and A. Tuel, *Appl. Catal., A*, 1996, **143**, 125.

22 X. X. Wang, F. Lefebvre, J. Patarin and J.-M. Basset, *Microporous Mesoporous Mater.*, 2001, **42**, 269.

23 M. S. Wong, H. C. Huang and J. Y. Ying, *Chem. Mater.*, 2002, **14**, 1961.

24 G. Mountjoy, D. M. Pickup, R. Anderson, G. W. Wallidge, M. A. Holland, R. J. Newport and M. E. Smith, *Phys. Chem. Chem. Phys.*, 2000, **2**, 2455.

25 J. Okabayashi, S. Toyoda, H. Kumigashira, M. Oshima, K. Usuda, M. Niwa and G. L. Liu, *J. Vac. Sci. Technol., A*, 2005, **23**, 1554.

26 A. M. Evans, J. P. H. Williamson and F. P. Glasser, *J. Mater. Sci.*, 1980, **15**, 2325.

27 W. D. Kingery, *Introduction to Ceramics*, John Wiley & Sons, New York, 1960.

28 S. Fabris, A. T. Paxton and M. W. Finnis, *Phys. Rev. B: Condens. Matter*, 2000, **61**, 6617.

29 L. Galoisy, E. Pélegrin, M. A. Arrio, P. Ildefonse, G. Calas, D. Ghaleb, C. Fillet and F. Pacaud, *J. Am. Ceram. Soc.*, 1999, **82**, 2219.

30 L. Cormier, O. Dargaud, G. Calas, C. Jousseaume, S. Papin, N. Trcera and A. Cognignia, *Mater. Chem. Phys.*, 2015, **152**, 41.

31 D. Ceresoli and D. Vanderbilt, *Phys. Rev. B: Condens. Matter*, 2006, **74**, 125108.

32 X. Luo, W. Zhou, S. V. Ushakov, A. Navrotsky and A. A. Demkov, *Phys. Rev. B: Condens. Matter*, 2009, **80**, 134119.

33 E. F. López, V. S. Escribano, M. Panizza, M. M. Carnasciali and G. Busca, *J. Mater. Chem.*, 2001, **11**, 1891.

34 P. E. R. Blanchard, S. Liu, B. J. Kennedy, C. D. Ling, Z. Zhang, M. Avdeev, B. C. C. Cowie, L. Thomsenc and L.-Y. Jangd, *Dalton Trans.*, 2013, **42**, 14875.

35 *X-Ray Absorption: Principles, Applications, Techniques of EXAFS, SEXAFS and XANES*, ed. D. C. Koningsberger and R. Prins, John Wiley & Sons, 1987.

36 J. J. Rehr and A. L. Ankudinov, *Coord. Chem. Rev.*, 2005, **249**, 131.

37 F. De Groot and A. Kotani, *Core Level Spectroscopy of Solids*, CRC Press, 2008.

38 E. L. Crepaldi, G. J. A. A. Soler-Illia, D. Grosso, P.-A. Albouy and C. Sanchez, *Chem. Commun.*, 2001, 1582.

39 E. L. Crepaldi, G. J. A. A. Soler-Illia, D. Grosso, F. Ribot, F. Cagnol and C. Sanchez, *J. Am. Chem. Soc.*, 2003, **125**, 9770.

40 P. C. Angelomé, L. Andrini, M. C. Fuertes, F. G. Requejo and G. J. A. A. Soler-Illia, *C. R. Chim.*, 2010, **13**, 256.

41 http://www.lnls.br (Instalações Abertas: Linhas de Luz: D11A-SAXS).

42 M. Abbate, F. C. Vicentin, V. Compagnon-Cailhol, M. C. Rocha and H. Tolentino, *J. Synchrotron Radiat.*, 1999, **6**, 964.

43 http://www.lnls.br (Instalações Abertas, Linhas de Luz, D04A-SXS).

44 D. A. Outka and J. Stöhr, *J. Chem. Phys.*, 1988, **88**, 3539.

45 T. Ressler, *J. Synchrotron Radiat.*, 1998, **5**, 118. http://www.winxas.de.

46 P. Innocenzi, *J. Non-Cryst. Solids*, 2003, **316**, 309.

47 M. Andrianainarivelo, R. Corriu, D. Leclercq, P. H. Mutin and A. Vioux, *J. Mater. Chem.*, 1996, **6**, 1665.

48 Z. Zhan and H. C. Zeng, *J. Non-Cryst. Solids*, 1999, **243**, 26.

49 J. M. Miller and L. J. Lakshmi, *J. Phys. Chem. B*, 1998, **102**, 6465.

50 S. H. Teo and H. C. Zeng, *J. Phys. Chem. B*, 2001, **105**, 9093.

51 S. D. Kelly, D. Hesterberg and B. Ravel, Analysis of soils and minerals using X-ray Absorption Spectroscopy, in *Methods of soil analysis*, ed. A. L. Ulery and L. R. Dress, 2008, vol. 5, pp. 387–463, SSSA Book Series.

52 H. Ikeno, M. Krause, T. Höche, C. Patzig, Y. Hu, A. Gawronski, I. Tanaka and C. Rüssel, *J. Phys.: Condens. Matter*, 2013, **25**, 165505.

53 P. Li, I.-W. Chen and J. E. Penner-Hahn, *Phys. Rev. B: Condens. Matter*, 1993, **48**, 10063; P. Li, I.-W. Chen and J. E. Penner-Hahn, *Phys. Rev. B: Condens. Matter*, 1993, **48**, 10074; P. Li, I.-W. Chen and J. E. Penner-Hahn, *Phys. Rev. B: Condens. Matter*, 1993, **48**, 10082.

54 B. N. Figgs and M. A. Hitchman, *Ligand Field Theory and its applications*, Wiley-VCH, N.Y., 2000.

55 J. P. Crocombette and F. Jollet, *J. Phys.: Condens. Matter*, 1994, **6**, 8341.

56 F. M. F. de Groot, Z. W. Hu, M. F. Lopez, G. Kaindl, F. Guillot and M. Tronc, *J. Chem. Phys.*, 1994, **101**, 6570.

57 F. M. F. de Groot, *Physica B*, 1995, **208–209**, 15.

58 C. Patzig, T. Höche, Y. Hu, H. Ikeno, M. Krause, M. Dittmer, A. Gawronski, C. Rüssel, I. Tanaka and G. S. Henderson, *J. Non-Cryst. Solids*, 2014, **384**, 47.

59 M. Morinaga, H. Adachi and M. Tsukada, *J. Phys. Chem. Solids*, 1983, **44**, 301.

60 R. H. French, S. J. Glass and F. S. Ohuchi, *Phys. Rev. B: Condens. Matter*, 1994, **49**, 5133.

61 J. C. Ballhausen, *Introduction to Ligand Field Theory*, McGraw-Hill, New York, 1962; B. N. Figgis, *Introduction to Ligand Field*, Malabar, Florida, 1986.

62 F. Alberts Cotton, *Chemical Applications of Group Theory*, Wiley-Interscience, New York, 3rd edn, 1990.

63 R. Burns, *Mineralogical Applications of Crystal Field Theory*, Cambridge University Press, New York, 1995.

64 For example, Ikeno *et al.*[52] demonstrated that four compounds of tetravalent Zr the coordination numbers and symmetries around the Zr ions are different.

65 E. Pelegrin, *Centre d'études de la Vallée du Rhône Site de Marcoul, RAPPORT CEA-R-5929*, Doctoral Thesis, Commissariat à l'EnergieAtomique, France, 2000.

66 J. J. Rehr, L. J. de Mustre, S. I. Zabinsky and R. C. Albers, *J. Am. Chem. Soc.*, 1999, **113**, 5135.

67 R. L. Mozzi and B. E. Warren, *J. Appl. Crystallogr.*, 1969, **2**, 164.

68 O. Dargaud, L. Cormier, N. Menguy, L. Galoisy, G. Calas, S. Papin, G. Querel and L. Olivi, *J. Non-Cryst. Solids*, 2010, **356**, 2928.

69 G. Mountjoy, R. Anderson, R. J. Newport and M. E. Smith, *J. Phys.: Condens. Matter*, 2000, **12**, 3505.

70 D. M. Pickup, G. Mountjoy, G. W. Wallidge, R. J. Newport and M. E. Smith, *Phys. Chem. Chem. Phys.*, 1999, **1**, 2527.

71 M. W. Gaultois, J. E. Greedan and A. P. Grosvenor, *J. Electron Spectrosc. Relat. Phenom.*, 2010, **184**, 192.

72 P. E. R. Blanchard, S. Liu, B. J. Kennedy, C. D. Ling, Z. Zhang, M. Avdeev, B. C. C. Cowie, L. Thomsen and L.-Y. Jangd, *Dalton Trans.*, 2013, **42**, 14875.

73 L. Cormier, O. Dargaud, G. Calas, C. Jousseaume, S. Papin, N. Trcera and A. Cognigni, *Mater. Chem. Phys.*, 2015, **152**, 41.

74 B. T. Thole and G. van der Laan, *Phys. Rev. B: Condens. Matter*, 1988, **38**, 1943; B. T. Thole and G. van der Laan, *Phys. Rev. B: Condens. Matter*, 1988, **38**, 3158.

75 D. Li, G. M. Bancroft, M. E. Fleet and X. H. Feng, *Phys. Chem. Miner.*, 1995, **22**, 15.

76 Prof. Dr Reinaldo Pis Diez, communication with the authors.